Point focusing with flat and wedged crossed multilayer Laue lenses

Adam Kubec,[a]* Kathleen Melzer,[b] Jürgen Gluch,[b] Sven Niese,[c] Stefan Braun,[a] Jens Patommel,[d] Manfred Burghammer[e] and Andreas Leson[a]

[a]Fraunhofer IWS Dresden, Winterbergstraße 28, 01277 Dresden, Germany, [b]Fraunhofer IKTS, Maria-Reiche-Straße 2, 01109 Dresden, Germany, [c]AXO DRESDEN GmbH, Gasanstaltstraße 8b, 01237 Dresden, Germany, [d]Institute of Structural Physics, Technische Universität Dresden, 01069 Dresden, Germany, and [e]ESRF, European Synchrotron Radiation Facility, Grenoble 30843, France. *Correspondence e-mail: adam.kubec@iws.fraunhofer.de
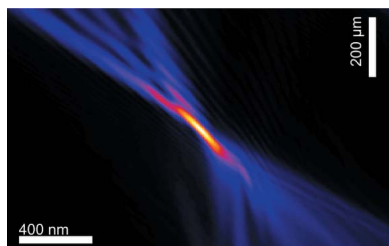
Point focusing measurements using pairs of directly bonded crossed multilayer Laue lenses (MLLs) are reported. Several flat and wedged MLLs have been fabricated out of a single deposition and assembled to realise point focusing devices. The wedged lenses have been manufactured by adding a stress layer onto flat lenses. Subsequent bending of the structure changes the relative orientation of the layer interfaces towards the stress-wedged geometry. The characterization at ESRF beamline ID13 at a photon energy of 10.5 keV demonstrated a nearly diffraction-limited focusing to a clean spot of 43 nm × 44 nm without significant side lobes with two wedged crossed MLLs using an illuminated aperture of approximately 17 µm × 17 µm to eliminate aberrations originating from layer placement errors in the full 52.7 µm × 52.7 µm aperture. These MLLs have an average individual diffraction efficiency of 44.5%. Scanning transmission X-ray microscopy measurements with convenient working distances were performed to demonstrate that the lenses are suitable for user experiments. Also discussed are the diffraction and focusing properties of crossed flat lenses made from the same deposition, which have been used as a reference. Here a focal spot size of 28 nm × 33 nm was achieved and significant side lobes were noticed at an illuminated aperture of approximately 23 µm × 23 µm.

1. Introduction

High-resolution X-ray imaging methods have become an important branch of non-destructive visualization in materials science and biological research (Wang *et al.*, 2014; Jakes *et al.*, 2015; Dehlinger *et al.*, 2015). Developments in micro-radiography and tomography enable imaging with resolution in the sub-micrometer range. Many of the current vital scientific questions require considerably higher spatial resolution and access to locally resolved spectroscopic information.

Various different X-ray imaging methods are established. Full-field X-ray microscopy allows for direct optical imaging at high spatial resolutions using high-performance optics. X-ray full-field imaging is realised with optical elements such as Fresnel zone plates at synchrotron radiation facilities (Rehbein *et al.*, 2009) as well as in laboratory instruments (Tkachuk *et al.*, 2006).

A large variety of characterization methods use a fine X-ray probe that is used to scan across a specimen. To achieve high spatial resolution a small spot size is required. In scanning transmission X-ray microscopy the transmitted intensity and its distribution are recorded to form an image. In fluorescence X-ray microscopy the emitted photon spectrum for each scan point gives information about the elemental composition.

Diffraction imaging methods such as ptychography benefit also from high-resolution optics because of the enhancement of the achievable resolution. Several types of focusing optics with spot sizes of less than 100 nm are used or have been demonstrated at synchrotron beamlines, such as KB mirrors (Mimura *et al.*, 2010), compound refractive lenses (Kurapova *et al.*, 2007) and Fresnel zone plates (Vila-Comamala *et al.*, 2011). These optics, however, have limitations regarding very high resolutions, practicability or efficiency. Multilayer Laue lenses (MLLs) (Maser *et al.*, 2004) and multilayer zone plates (Rudolph & Schmahl, 1980; Rudolph *et al.*, 1982) were proposed to overcome several physical and technical limitations connected to the previously mentioned lenses. Based on the principle of diffraction, MLLs are basically linear zone plates made by thin-film technologies. Compared with Fresnel zone plates smaller zone widths can be manufactured and allow for higher spatial resolutions. Due to the sectioning process with focused ion beam milling, any desired aspect ratio can be fabricated to achieve optimal efficiencies. Consequently, MLLs are predicted to achieve subnanometer spot sizes with high efficiencies (Schroer *et al.*, 2005; Yan *et al.*, 2014).

The zones are deposited with individual layer thicknesses according to the approximated zone plate law $r_n^2 = n\lambda f$. The approximation is valid for $f \gg (n\lambda)/2$ (Attwood, 2007). r_n is the distance of the nth zone from the optical axis, λ is the wavelength and f is the focal length. The term radius will be used analogously for Fresnel zone plates, *i.e.* the optical axis is located at $r = 0$. A certain radius can also be unambiguously matched to a certain zone width for a given zone plate design. Several types of MLLs have been defined (Yan *et al.*, 2007b); usually the zones of an MLL are located only on one side of the optical axis and inner zones are omitted in the fabrication process. This type is referred to as a partial MLL and by definition represents an off-axis optical system. A half MLL is a structure where all zones on one side of the optical axis are manufactured and a full MLL corresponds to a Fresnel zone plate geometry with zones symmetrically distributed on both sides of the optical axis. Yan & Chu (2013) showed that, as a result of the intercept theorem, a partial MLL has a slightly larger working distance than a full MLL with a beamstop for otherwise identical parameters of the aperture size and the focal length. The working distance equals the distance from the order sorting aperture to the focal plane. In addition, there is no apodization effect caused by a central beam stop in the case of a partial MLL. As well as these types, several MLL geometries exist which differ mainly in the alignment and shape of the layer interfaces. An MLL with layer interfaces parallel to the optical axis is called a flat MLL. A partial MLL can be tilted to improve the efficiency of the lens by exploiting the Bragg condition in a part of the lens [Figs. 1 (*a*) and 1(*b*)]. Ideally, all zones should comply with their local Bragg condition, which is not possible if the interfaces of the zones are parallel as the Bragg angle of the structure increases linearly as a function of the radius in terms of the zone plate law (Kang *et al.*, 2006). The ideal shape for a diffractive transmission optic to focus an incident plane wave is a cut
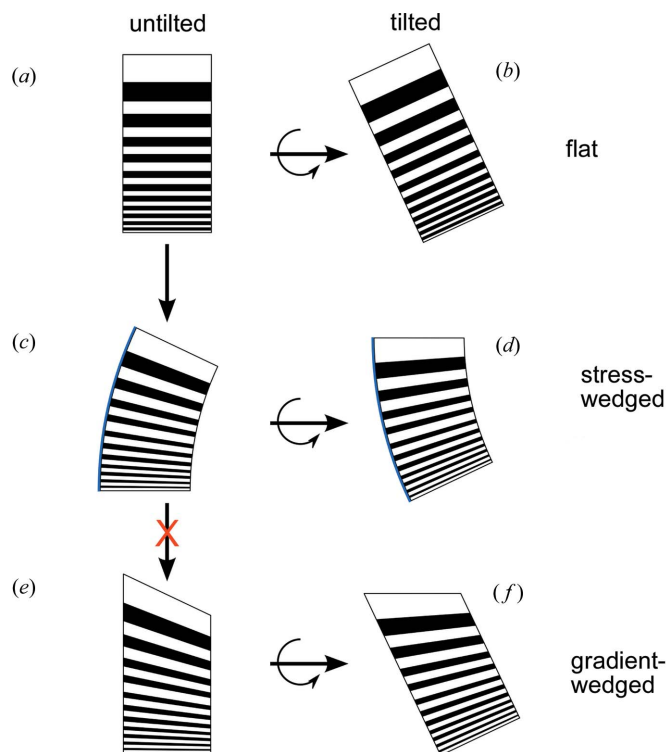

Figure 1
MLL geometries. The left-hand views show the manufactured shapes of the lens and the right-hand views show the geometry usually used for experiments: (*a*) flat geometry, (*b*) tilted geometry, (*c*) stress-wedged geometry, (*d*) tilted stress-wedged geometry, (*e*) gradient-wedged geometry and (*f*) tilted gradient-wedged geometry. The geometries shown in (*e*) and (*f*) have not been used in the scope of this work and are discussed for comparison. In this scheme an incident beam is coming from the left side and would be focused to the right side. From a flat lens either a tilted or a stress-wedged MLL is obtained. The gradient-wedged MLL has to be manufactured from a dedicated deposition with a steep lateral thickness gradient. The arrows indicate possible changes between geometries.

through a set of confocal paraboloids (Yan *et al.*, 2007b). This geometry is called a curved MLL. An approximation where the interfaces of the zones are linearly pointing to one single point is called wedged geometry. To achieve small focal spot sizes it is necessary to build lenses with a large numerical aperture. In the case of MLLs, the total thickness of the deposited multilayer stack corresponds to the aperture D of the lens. Therefore, it is necessary to manufacture a multilayer stack with a large total thickness consisting of thousands of individual layers in order to achieve a large numerical aperture at practicable focal lengths and working distances.

Most of the material combinations in use for MLLs have inherent stress. The stress accumulates with increasing total deposition thicknesses and may lead to severely deformed or broken substrates at total deposition thicknesses above 50 µm. Currently, several groups are approaching the challenges of building lenses with total deposition thicknesses exceeding 50 µm and several approaches have been discussed to reduce the strain or its impact on the multilayer structure (Shi *et al.*, 2014; Braun *et al.*, 2015). Recently total deposition thicknesses of about 50 µm and 100 µm have been demonstrated (Kubec *et al.*, 2014; Macrander *et al.*, 2015). To obtain an undistorted

focus a good agreement of the individual layer thicknesses with the zone plate law is necessary. Therefore, it is essential to fabricate such a stack without any significant local and global layer placement errors. The effects of different kinds of layer placement error are discussed by Yan *et al.* (2007*a*), Liao *et al.* (2014) and Andrejczuk *et al.* (2015). A deposition process with good stability and knowledge about its long-term behavior is required to avoid such effects. To obtain a focusing element, the multilayer stack is machined to a slice with a section thickness according to the material combination and the desired X-ray photon energy (referred to as design photon energy). This can be perfomed using various techniques (Kang *et al.*, 2007; Kubec *et al.*, 2014).

To fabricate a wedged MLL (wMLL) two main approaches have been used so far. One is using a shadow mask for blocking the material flux on the substrate during the deposition process to obtain a rather steep total deposition thickness gradient of the whole multilayer stack along a vector parallel to the substrate surface (Conley *et al.*, 2008; Huang *et al.*, 2015; Morgan *et al.*, 2015). Another approach is manufacturing a flat MLL and adding a stress layer onto one side of the structured optical element (Niese *et al.*, 2014*b*). The resulting shape of the lens can be seen in Figs. 1(*e*) and 1(*c*). The latter manufacturing approach has been used for the lenses discussed here. If a distinction is necessary we will call these lenses *gradient-wedged* MLL and *stress-wedged* MLL, respectively.

The stress-wedged MLL is a different approach to achieve similar results as a gradient-wedged MLL. A gradient-wedged MLL requires a very steep gradient with a slope of $D/(2f)$ to be manufactured. The properties of the resulting wedge have to be known precisely to be able to extract the MLL at the correct position of the wedge for a specific photon energy. Due to the shadowing effect of the mask the deposition flux is reduced. This results in even longer deposition times for a specific thickness as compared with a flat geometry.

Stress-wedged MLLs are made similarly to a flat geometry lens. Subsequently, an SiO_2 stress layer is deposited on the side facing the incoming X-ray beam. Due to the compressive stress of the SiO_2 layer, the whole structure is bent uniformly. In this way the layer interfaces are no longer parallel and imitate the curved geometry. For a flat MLL the focal length varies linearly with the photon energy. Using a stress layer, such an MLL can be optimized for a specific photon energy independently from the actual MLL deposition. The bending can be estimated by numerical calculations. Necessary material parameters such as Young's modulus are well known for bulk materials. However, for thin-film stacks they have only been estimated. Therefore, calibration measurements have to be made in order to find good parameters for the calculations.

A single MLL is a line focusing element; two lenses have to be aligned perpendicularly behind each other to achieve a point focus. Experimental point focusing results achieved with such crossed MLLs are discussed by Yan *et al.* (2011) and Kubec *et al.* (2014).

2. MLL fabrication and in-house characterization

The individual layer thicknesses of the deposition were calculated with the zone plate law for a focal length of 9.5 mm at an X-ray photon energy of 15 keV. Zones 850 to 7850 were chosen; this results in zone widths between 5.00 nm and 15.19 nm. This results in an aperture of 52.7 µm representing zone plate law radii between 25.8 µm and 78.5 µm. The resulting working distance is 3.1 mm at this photon energy. A very small thickness gradient along a vector parallel to the substrate surface is used for matching focal lengths of the two separate lenses. Owing to the planetary movement in the deposition chamber, this gradient has a radial direction (Kubec *et al.*, 2014).

The multilayer was fabricated by magnetron sputter deposition in a rotary deposition machine (Braun *et al.*, 2002). A commercially available silicon substrate was coated with alternating layers of amorphous Si and WSi_2. We experienced inherent stress in the deposited multilayer stack, which led to a significant and unwanted bending of the substrate. For characterizing stress measurements we have used an FLX 2320 by Toho Technology Corporation. However, the stress of the MLL deposition could not be measured due to the large polyaxial bending of the substrate.

This indicates that a further increase in the stack thickness without improvements of the stress management will result in breakage of the substrate.

Information about the layer placement error was obtained by measuring the distance of marker layers in the MLL using scanning electron microscopy (Conley *et al.*, 2012). The measurement of the distances between the marker layers in comparison with the design values for the segments is shown in Fig. 2(*a*). A gradient of deviation between measurement and design of approximately 1% is visible between the innermost radius and approximately $r = 65$ µm. From there up
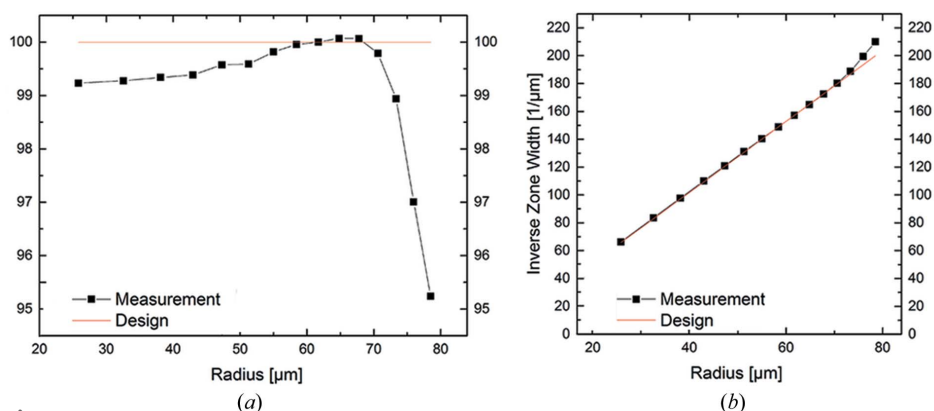

Figure 2
(*a*) Relative deviation of the measured layer thickness as a function of the radius. (*b*) Spatial frequency of the zones as a function of the radius. The red lines indicate the design values.

Table 1
Individual lenses used in this experiment.

Lenses fabricated from a WSi_2/Si deposition with an aperture of 53.7 µm (zones 850–7850) and a diffraction-limited focal size of 13.1 nm and a focal length of f = 9.5 mm at 15 keV.

ID	Geometry	Section thickness (µm)
#1	Flat	8.1
#2	Flat	4.5
#3	Flat	4.7
#4	Wedged	8.0
#5	Wedged	7.0

Figure 3
(a) SEM image of a wedged MLL with a box showing the position of the tilt map. (b) Relative tilt map for MLL #4, approximately 0.77 mrad µm^{-1}. (c) Relative tilt map for MLL #5, approximately 0.75 mrad µm^{-1}.

to the outermost radius the deviation increases and reaches up to 5% from the design values. In the spatial frequency representation shown in Fig. 2(b) a deviation of up to 5% at radii above approximately 65 µm is very noticeable. A deviation of up to 1% at smaller radii seems far less visible as compared with the design values. Therefore, the authors conclude that the representation in Fig. 2(a) is more useful in order to make the global deviations quantitatively visible. The evaluation is based on the measurement of the distance between the marker layers. Thus, both representations are not well suited in order to detect one or multiple single layer (e.g. caused by arcs during the deposition process) or stochastic errors. These errors might also result in aberrations, which can have severe impact on the focal spot (Andrejczuk et al., 2015). The discussed type of layer thickness analysis has to be supplemented with other methods in order to gain a full image of the layer properties. Therefore not the entire part of the lens, which has been judged to be flawless by this kind of SEM analysis, might be suited for focusing applications.

To produce the lens elements an approach very similar to the preparation of H-bar lamella for TEM samples was established. Therefore, a wafer with the multilayer deposition was cleaved and stripes with a width of approximately 80 µm were cut with an automatic dicing saw (DAD 321, DISCO Corporation).

These stripes were then processed by focused ion beam milling (Zeiss NVision 40) to obtain MLLs with the desired section thicknesses of 4 µm and 8 µm. A section thickness of 4 µm was chosen for the flat MLLs in crossed geometry to minimize volume diffraction effects and to obtain a better focal spot. This is smaller than the calculated section thickness necessary for optimal diffraction efficiency using the two-beam approximation. For the wMLL, a section thickness of 8 µm for significant volume diffraction was chosen in order to obtain optimal diffraction efficiency. An additional 8 µm-thick flat MLL was fabricated as a reference. In total five different individual lenses have been used in the scope of this work (see Table 1), hereafter referred to as MLL #1 to MLL #5.

To obtain the stress-wedged geometry a 200 nm-thick SiO_2 stress layer was deposited using ion beam sputter deposition (Gawlitza et al., 2006) on the lens side facing the beam (Niese et al., 2014b). Identical stress layers have been deposited on vertical and horizontal MLLs of the crossed MLL system.

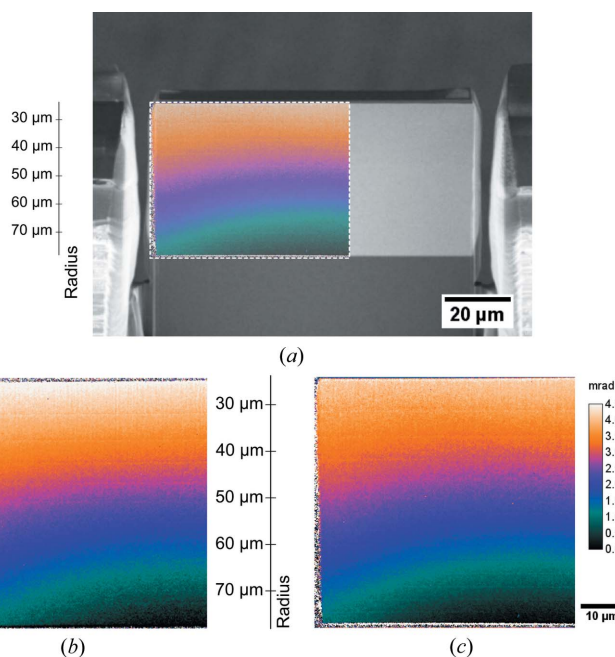The relative layer tilt was measured in a laboratory-based X-ray microscope (Xradia NanoXCT-100) with the method described by Niese et al. (2014b). The resulting curvature is shown in Fig. 3; measured curvatures of 0.077 mrad µm^{-1} and 0.075 mrad µm^{-1} for MLL #4 and MLL #5, respectively, were too large for the originally intended photon energy of 15 keV. It matches to a photon energy of 10.5 keV. At this photon energy the corresponding focal length is reduced to 6.65 mm and the working distance is reduced to 2.2 mm. It is expected that a better matching of the curvature can be achieved by improved calibration experiments.

Two matching lens elements for vertical and horizontal focusing are mounted perpendicularly onto a single lens holder, designed for integration in the ESRF beamline ID13. The distance in beam direction between both lens elements is less than 50 µm and, thus, significantly smaller than the focal length (Niese et al., 2014a). The degree of wedging for both lenses has to be nearly identical due to the small relative distance. Owing to the similar numerical aperture, the size of the focus is expected to be comparable in both horizontal and vertical directions. The relative angular alignment requires high precision; according to Yan et al. (2008) the maximum tolerable deviation is of the order of 0.5 mrad for our setup.

3. Experiments and results

We present the experimental results of measurements of three single lenses and two pairs of lenses. Synchrotron radiation experiments have been performed at the ESRF beamline ID13 with a photon energy of 10.5 keV. The nanofocusing refractive lenses, which are mounted in the setup for user experiments (Schroer et al., 2005), were replaced by the MLLs. For the experiment with MLLs a custom lens mount and a
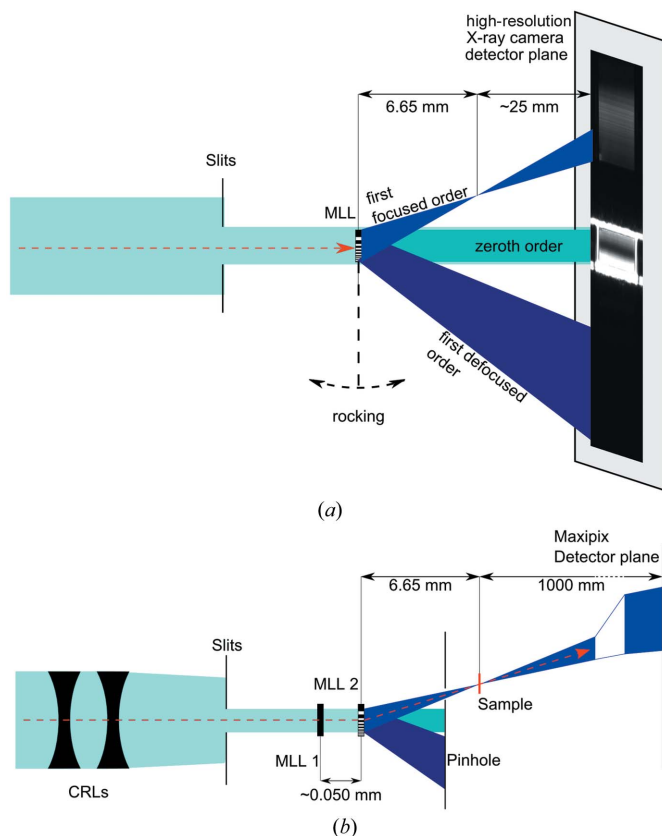
non-zero diffraction orders are separated from the direct beam in the image plane.

Fig. 5 shows a direct comparison of the transmission and diffraction patterns of flat and wedged MLLs for several angles. In Fig. 5(a) the pattern of the tilted flat MLL #1 is shown. It is evident that the Bragg condition is only fulfilled in a small part of the lens for a given angle. In zeroth-order transmission a dark band parallel to the interfaces is visible inside the aperture of the MLL. The bright band in the diffracted beam represents the particular part of the lens that is currently diffracting. On the other hand, for the wedged MLL #4 in Fig. 5(b), it is evident that the transmission inside the lens is reduced nearly equally across the whole aperture. A corresponding plateau is observed inside the diffraction pattern. Owing to the significant layer placement error, a part of the lens shows a noticeably lower intensity, *i.e.* the intensity is wrongly distributed in this part of the diffraction pattern. For this part the Bragg condition of the layers does not correspond very well with the actual tilting angle. From this type of measurement it is not possible to draw direct conclusions regarding the focal spot size or its shape (Andrejczuk *et al.*, 2015).

The measured intensity perpendicular to the layer orientation is plotted as a function of the rocking angle similar to those reported by Koyama *et al.* (2008), Kubec *et al.* (2015) and Morgan *et al.* (2015). Fig. 6 shows the results for both wedged lenses and the flat reference lens.

The upper part of the Fig. 6 shows the relevant first focused order. For the flat lens, only a part of the lens shows significant diffraction. Both wedged lenses yield a significantly more homogeneous first-order diffraction along the entire aperture. Corresponding shifts are observed for the first defocused
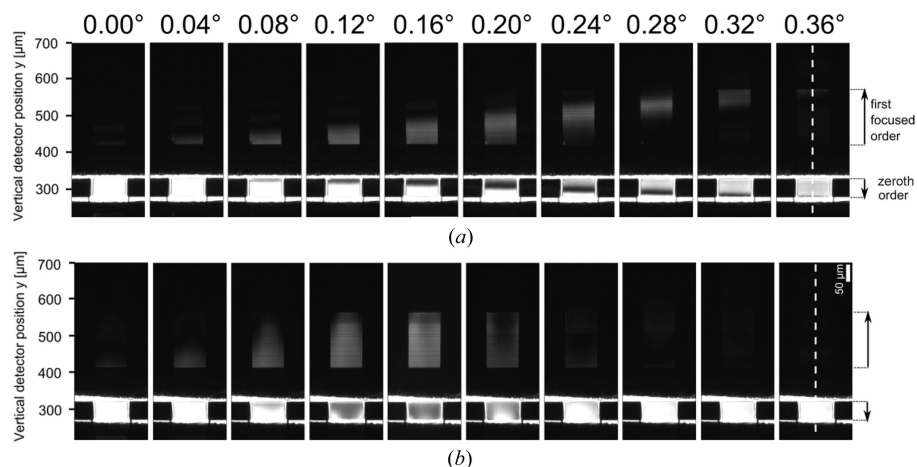

Figure 4
(a) Setup for the one-dimensional experiment with one lens. (b) Setup for point focusing; two compound refractive lenses were used for prefocusing to enhance the flux on the MLLs. Not to scale; photon energy is 10.5 keV.

custom pinhole were used, which have both been mounted into the existing optics setup at the beamline. No further modifications of the beamline were necessary.

3.1. Analysis of rocking series of single MLLs obtained with a high-resolution X-ray camera in close distance

In a first step the zeroth-order transmission and first-order diffraction, in particular, of otherwise identical wedged and flat lenses were compared (MLL #1 and MLL #4). Each lens was tilted to its respective Bragg condition. These measurements and the alignment were made with a high-resolution imaging X-ray microscope with a PCO 4000 camera. The scintillator was placed approximately 25 mm downstream of the focal plane. The setup of the experiments is shown in Fig. 4(a). Horizontal slits were used to truncate the illumination to an area somewhat larger than the MLL aperture. Hence,

Figure 5
Direct comparison of the transmission through the lens and diffraction into the first focused order of (a) a flat (MLL #1) and (b) a wedged MLL (MLL #4) for angles from 0° to 0.36°. The angle of the maximum diffracted intensity is 0.16° and 0.20° for the wedged and flat lens, respectively. For the wedged lens it is evident that the transmitted intensity is almost uniformly distributed over the aperture of the entire wedged lens, which is also true for the diffracted beam except for the part representing the significant layer placement error. Contrast has been reduced to 15% for better display of the effects. The measurement was made in the near field with the situation shown in Fig. 4(a). The dashed line in the rightmost images represents the axis, which was used for the construction of the representation in Fig. 6. Vertical detector position coordinates correspond to the vertical detector position coordinates in Fig. 6.
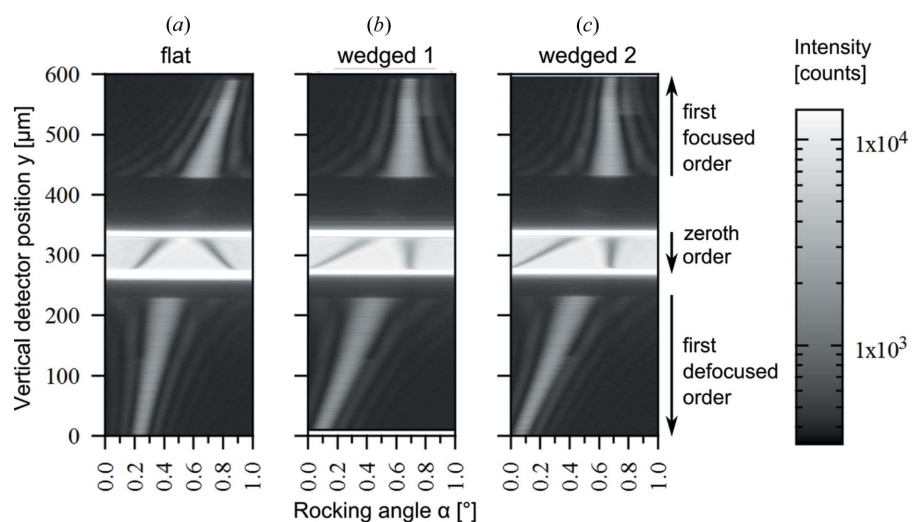
Figure 6
Intensity on the detector as a function of the rocking angle in logarithmic scale of one flat and two wedged MLLs as a function of the rocking angle including the transmitted beam and both focused and defocused first diffraction orders. The graphs show the measured intensity as a function of the rocking angle and the vertical detector position. The corresponding horizontal detector position is indicated with dashed lines in Fig. 5 for one rocking angle. View (a) represents the flat MLL #1 as a reference. Views (b) and (c) represent the results for the wedged MLL #4 and MLL #5, which were later on assembled for point focusing. The upper part shows the first focused order, the lower part the first defocused order; the central part shows the transmission through the lens. The arrows on the right show the direction of increasing radii similar to those in Fig. 5. Measurement was made in the near field with the setup as shown in Fig. 4(a).

of 100 ms and a detector distance of 1 m. For these experiments only a part of the MLL was illuminated, while the rest was masked by the illumination slits. The illuminated part of the aperture will be referred to as the *illuminated aperture*. The experimental setup is shown in Fig. 4(b).

Several ptychography measurements have been made for the lenses to test the impact of the layer placement error on different radii and to find the best position and size of the illumination for the best focusing results. For the flat lenses the largest illuminated aperture possible with reasonable side lobes was determined to be approximately 23 μm × 23 μm. Line profiles through the point with the maximum intensity from the best illumination are shown in Fig. 7. The full width at half-maximum (FWHM) size was determined by a $sinc^2$ function being fitted to the line profiles of the reconstructed foci. A $sinc^2$ function represents the ideal point spread function for a rectangular aperture (Born & Wolf, 1999). The FWHM of

order seen in the lower part of Fig. 6. A larger shift is observed for the wedged MLLs due to their optimization for the first focused order. A similar pattern of dark bands is seen in zeroth-order transmission in the central part of Fig. 6.

Due to the layer placement error a slight kink and a change in intensity on the detector can be noticed for that part representing the outermost zones.

3.2. Focus characterization of crossed MLLs by ptychography

We obtained detailed information about the focusing capabilities from ptychography reconstructions (Hönig *et al.*, 2011). Ptychography is a scanning imaging technique, where a sample is scanned with overlapping illuminations. From far-field diffraction patterns amplitude and phase of the sample and the complex wavefield of the illumination in the object plane can be reconstructed. This information is used to obtain information about the position of the focal plane relative to the sample and, more important, of the relative misalignment of the lenses (Braun *et al.*, 2013; Kubec *et al.*, 2014).

A Siemens star test pattern (NTT-AT ATN/XRESO-50HC) with 500 nm-thick tantalum features with lines and spaces down to a size of 50 nm was used as a sample. An area of 1.6 μm × 1.6 μm was scanned with a step size of 40 nm and a dwell time

the focal profiles are 28 nm and 33 nm, respectively. This approximately corresponds to the diffraction-limited spot size for the illuminated aperture. The difference in focal sizes in both directions is probably due to different tilting angles for horizontal and vertical lenses, respectively, which can have an impact on the focal size (Yan *et al.*, 2007b). Side lobes are more pronounced than expected for our MLLs. It was shown that side lobes are more pronounced if the angle of the lens is not perfectly aligned and in addition the present layer placement error might lead to a further increase of the intensity in the side lobes (Yan *et al.*, 2007a).

Using wedged MLLs we found the best focus in terms of spot size and the intensity in the side lobe using an illuminated aperture of approximately 15 μm × 15 μm as given by the encoders of the slit motors. The focus from this part of the lens was determined by ptychography to have an FWHM of 43 nm
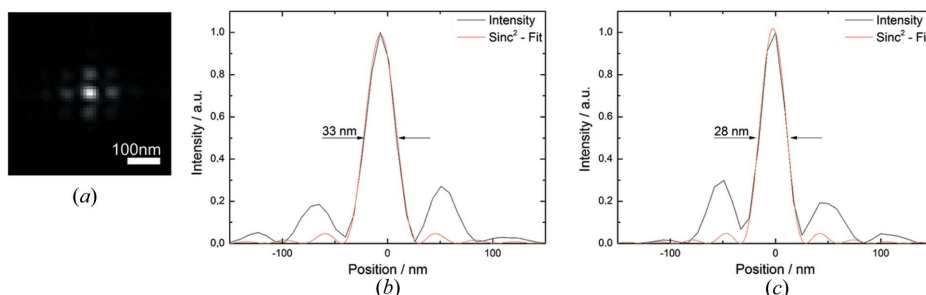

Figure 7
(a) Focal spot and focal profiles for (b) horizontal and (c) vertical directions of the pair of flat crossed MLLs with an illuminated aperture of 23 μm × 23 μm as reconstructed from ptychography measurements.
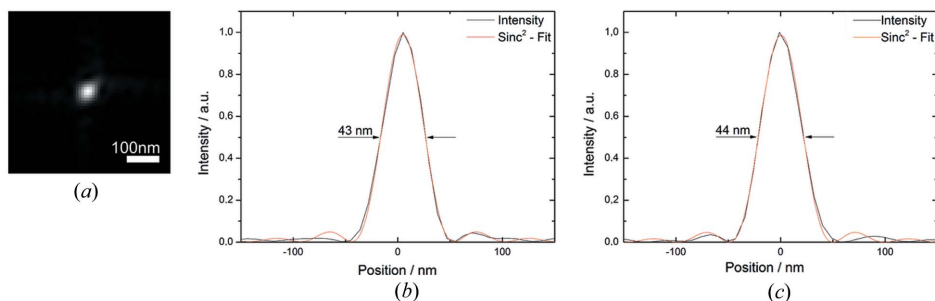
Figure 8
(a) Focal spot and focal profiles for (b) horizontal and (c) vertical directions of the pair of wedged crossed MLLs with an illuminated aperture of 15 µm × 15 µm as reconstructed from ptychography measurements.
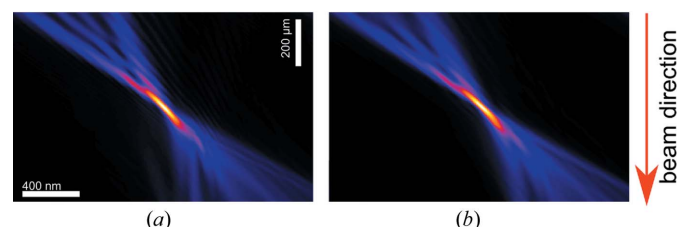

Figure 9
Reconstructed caustic in (a) horizontal and (b) vertical directions for the crossed wedged MLL as reconstructed from ptychography measurements.
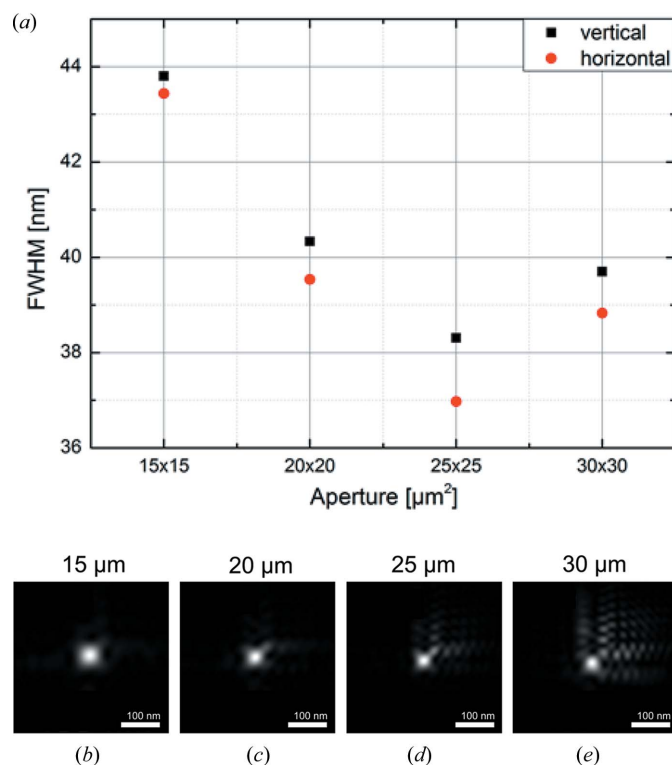

Figure 10
(a) Focal spot size as a function of illuminated aperture of the crossed wedged MLL as reconstructed from ptychography measurements. (b)–(e) Corresponding intensity distribution in the focal plane for different illuminated aperture edge lengths. For apertures larger than 15 µm × 15 µm the effect of the layer placement error becomes more significant.

× 44 nm (see Fig. 8). Fig. 9 shows the reconstructed caustic of both the horizontal and the vertical focusing directions. The size of the beam corresponds to an aperture of approximately 16.8 µm. Therefore, we assume that the focus size is nearly diffraction-limited with respect to the illuminated aperture. For further experiments we used this setup, as it is very close to the expected point spread function for this type of lens.

For larger illuminated apertures slightly smaller central feature sizes have been obtained (Fig. 10a). The smallest focus size achieved was 37 nm × 38 nm; shapes and sizes in the estimated focal planes are shown in Fig. 10. The influence of the layer placement error is insignificant for an illuminated aperture up to 16.8 µm in the case of the wedged geometry. Its influence becomes apparent if larger illuminated apertures are used for focusing. Compared with the tilted geometry a different behavior might be expected for the same layer placement error. Owing to the more inhomogeneous local diffraction efficiency of the tilted geometry the effect of the same layer placement error might appear different. It seems that a layer placement error is less tolerable for wedged MLLs than for tilted MLLs in terms of the resulting focus size.

We have used the setup as presented in Fig. 4(b) for scanning transmission measurements of the Siemens star test sample. A comparison between the scanning X-ray transmission experiments and the respective ptychography measurements with the same setup is shown in Fig. 11. Ideally the test sample would absorb 15.8% of the beam [according to the absorption data reported by Henke *et al.* (1993)]. According to the measured contrast between transmitted and absorbed beam, the difference between expected and measured values is negligible. There are no features indicating smearing. This shows that no significant side lobes are present and confirms the quality of the focal spot obtained from the ptychography measurements.
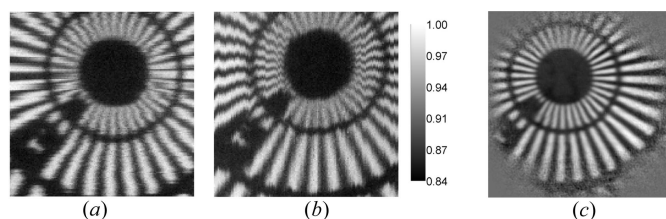

Figure 11
(a, b) Scanning transmission measurements with a PIN-diode of the same region of the Siemens star with the wedged MLL as focusing optics. Fast scanning axis is horizontal and vertical, respectively. The grayscale shows the transmitted intensity of the beam. (c) The reconstructed phase image of the same region of the test sample. Measurement was made with the setup shown in Fig. 4(b).

Table 2
Tabular summary of the measured efficiencies η for both types of lenses.

MLL type	Section thicknesses	η^2 (%)	η (%)
Flat (#2/#3)	4.5/4.7	7.9	28.2
Wedged (#4/#5)	7.0/8.0	19.8	44.5

3.3. Efficiency measurements

We measured the efficiency of the crossed lenses by measuring the photon flux using a calibrated PIN-diode for a given slit width, lens and aligned pinhole and compared it with the flux without a lens and without a pinhole. The results give the efficiency of the combination of vertical and horizontal lenses. The efficiency of one single lens element is estimated by assuming that both lenses diffract equally; individual efficiencies are estimated by the square root of the combined efficiency. Results are listed in Table 2. Based on the results we do not expect any significant loss in efficiency or an introduction of significant aberrations from the stress layer on account of its small layer thickness and low absorption of SiO_2. For the wMLL the measured efficiency was nearly equal across the entire aperture proving that the lens was manufactured and aligned well. The expected efficiency calculated by the two-beam approximation is 49% and, thus, only slightly larger than the measured value of 44.5%. The calculated results from the two-beam approximation are rather overestimating the expected efficiency as other orders than the first focused orders are neglected (Yan *et al.*, 2014). Therefore, we can assume that we are quite close to the expected efficiencies for this material system at 10.5 keV.

A further improvement in diffraction efficiency can be achieved by the use of a different material system. An MLL made of a multilayer material system with a molybdenum-based absorber can achieve an efficiency of up to about 70% at a photon energy of 10.5 keV (Kubec *et al.*, 2016).

4. Conclusion and outlook

We have deposited a stack for multilayer Laue lenses made of Si and WSi_2 with a structure corresponding to 7000 zones on a flat substrate with individual layer thicknesses closely matching the zone plate law and with a total design thickness of 53.7 μm. From this deposition several flat and wedged multilayer Laue lenses have been manufactured. We have demonstrated point focusing with crossed wedged multilayer Laue lenses, which were fabricated by adding a stress layer to a flat geometry lens. The results were compared with a pair of flat MLLs made from the same deposition.

Experiments at a photon energy of 10.5 keV have shown focal spot sizes with the FWHM significantly less than 50 nm in both focusing directions as reconstructed from ptychography. For the wedged lenses scanning transmission measurements confirm the small focal spot size; a combined efficiency of 19.8% for both serial lenses and an individual efficiency of 44.5% for the single lenses was determined, which is significantly higher than previous measurements with tilted

and wedged MLLs and which is close to the theoretically expected values.

Whereas the layer placement error was identified as the reason for significant side lobes, using a smaller part of the lens shows a nearly diffraction-limited point focus with only weak side lobes. By increasing the size of the illuminated aperture with a better matching of the zone plate law it is expected that even smaller focal spot sizes may be achieved. Alternative material systems will allow for higher efficiencies at relevant energies. The experiments also have shown the practicability of stress-wedging. As the photon energy had to be adjusted as compared with the intended energy it is also evident that the manufacturing method needs further calibration in order to make the process of wedging available for a predetermined energy.

References

Andrejczuk, A., Krzywinski, J. & Bajt, S. (2015). *Nucl. Instrum. Methods Phys. Res. B*, **364**, 60–64.

Attwood, D. (2007). *Soft X-rays and Extreme Ultraviolet Radiation: Principles and Applications.* Cambridge University Press.

Born, M. & Wolf, E. (1999). *Principles of Optics*, 7th (expanded) ed. Cambridge University Press.

Braun, S., Kubec, A., Gawlitza, P., Menzel, M. & Leson, A. (2015). *Proc. SPIE*, **9510**, 95100L.

Braun, S., Kubec, A., Menzel, M., Niese, S., Krüger, P., Seiboth, F., Patommel, J. & Schroer, C. (2013). *J. Phys. Conf. Ser.* **425**, 052019.

Braun, S., Mai, H., Moss, M., Scholz, R. & Leson, A. (2002). *Jpn. J. Appl. Phys.* **41**, 4074.

Conley, R., Bouet, N., Zhou, J., Yan, H., Chu, Y., Lauer, K., Miller, J., Chu, L. & Jahedi, N. (2012). *Proc. SPIE*, **8502**, 850202.

Conley, R., Liu, C., Qian, J., Kewish, C. M., Macrander, A. T., Yan, H., Kang, H. C., Maser, J. & Stephenson, G. B. (2008). *Rev. Sci. Instrum.* **79**, 053104.

Dehlinger, A., Blechschmidt, A., Grötzsch, D., Jung, R., Kanngiesser, B., Seim, C. & Stiel, H. (2015). *Proc. SPIE*, **9589**, 95890M.

Gawlitza, P., Braun, S., Lipfert, S. & Leson, A. (2006). *Proc. SPIE*, **6317**, 63170G.

Henke, B. L., Gullikson, E. M. & Davis, J. C. (1993). *At. Data Nucl. Data Tables*, **54**, 181–342.

Hönig, S., Hoppe, R., Patommel, J., Schropp, A., Stephan, S., Schöder, S., Burghammer, M. & Schroer, C. G. (2011). *Opt. Express*, **19**, 16324–16329.

Huang, X., Conley, R., Bouet, N., Zhou, J., Macrander, A., Maser, J., Yan, H., Nazaretski, E., Lauer, K., Harder, R., Robinson, I. K., Kalbfleisch, S. & Chu, Y. S. (2015). *Opt. Express*, **23**, 12496–12507.

Jakes, J. E., Hunt, C. G., Yelle, D. J., Lorenz, L., Hirth, K., Gleber, S.-C., Vogt, S., Grigsby, W. & Frihart, C. R. (2015). *Appl. Mater. Interfaces*, **7**, 6584–6589.

Kang, H., Maser, J., Stephenson, G., Liu, C., Conley, R., Macrander, A. & Vogt, S. (2006). *Phys. Rev. Lett.* **96**, 127401.

Kang, H. C., Stephenson, G. B., Liu, C., Conley, R., Khachatryan, R., Wieczorek, M., Macrander, A. T., Yan, H., Maser, J., Hiller, J. & Koritala, R. (2007). *Rev. Sci. Instrum.* **78**, 046103.

Koyama, T., Ichimaru, S., Tsuji, T., Takano, H., Kagoshima, Y., Ohchi, T. & Takenaka, H. (2008). *Appl. Phys. Expr.* **1**, 117003.

Kubec, A., Braun, S., Gawlitza, P., Menzel, M. & Leson, A. (2016). *AIP Conf. Proc.* **1741**, 040010.

Kubec, A., Braun, S., Niese, S., Krüger, P., Patommel, J., Hecker, M., Leson, A. & Schroer, C. G. (2014). *J. Synchrotron Rad.* **21**, 1122–1127.

Kubec, A., Kujala, N., Conley, R., Bouet, N., Zhou, J., Mooney, T. M., Shu, D., Kirchman, J., Goetze, K., Maser, J. & Macrander, A. (2015). *Opt. Express*, **23**, 27990–27997.

Kurapova, O., Lengeler, B., Schroer, C., Küchler, M., Gessner, T. & van der Hart, A. (2007). *J. Vac. Sci. Technol. B*, **25**, 1626–1629.

Liao, K., Hong, Y., Wang, Q., Chang, G. & Sheng, W. (2014). *Opt. Commun.* **325**, 111–115.

Macrander, A. T., Kubec, A., Conley, R., Bouet, N., Zhou, J., Wojcik, M. & Maser, J. (2015). *Appl. Phys. Lett.* **107**, 081904.

Maser, J., Stephenson, G. B., Vogt, S., Yun, W., Macrander, A., Kang, H. C., Liu, C. & Conley, R. (2004). *Proc. SPIE*, **5539**, 185–194.

Mimura, H., Handa, S., Kimura, T., Yumoto, H., Yamakawa, D., Yokoyama, H., Matsuyama, S., Inagaki, K., Yamamura, K., Sano, Y., Tamasaku, K., Nishino, Y., Yabashi, M., Ishikawa, T. & Yamauchi, K. (2010). *Nat. Phys.* **6**, 122–125.

Morgan, A. J., Prasciolu, M., Andrejczuk, A., Krzywinski, J., Meents, A., Pennicard, D., Graafsma, H., Barty, A., Bean, R. J., Barthelmess, M., Oberthuer, D., Yefanov, O., Aquila, A., Chapman, H. N. & Bajt, S. (2015). *Sci. Rep.* **5**, 9892.

Niese, S., Krüger, P., Kubec, A., Braun, S., Patommel, J., Schroer, C. G., Leson, A. & Zschech, E. (2014a). *Opt. Express*, **22**, 20008–20013.

Niese, S., Krüger, P., Kubec, A., Laas, R., Gawlitza, P., Melzer, K., Braun, S. & Zschech, E. (2014b). *Thin Solid Films*, **571**, 321–324.

Rehbein, S., Heim, S., Guttmann, P., Werner, S. & Schneider, G. (2009). *Phys. Rev. Lett.* **103**, 110801.

Rudolph, D., Niemann, B. & Schmahl, G. (1981). *Proc. SPIE*, **0316**, 103–105.

Rudolph, D. & Schmahl, G. (1980). *Ann. NY Acad. Sci.* **342**, 94–104.

Schroer, C. G., Kurapova, O., Patommel, J., Boye, P., Feldkamp, J., Lengeler, B., Burghammer, M., Riekel, C., Vincze, L., van der Hart, A. & Küchler, M. (2005). *Appl. Phys. Lett.* **87**, 124103.

Shi, B., Macrander, A. T., Maser, J., Conley, R. & Assoufid, L. (2014). *Proc. SPIE*, **9207**, 920708.

Tkachuk, A., Feser, M., Cui, H., Duewer, F., Chang, H. & Yun, W. (2006). *Proc. SPIE*, **6318**, 63181D.

Vila-Comamala, J., Gorelick, S., Färm, E., Kewish, C. M., Diaz, A., Barrett, R., Guzenko, V. A., Ritala, M. & David, C. (2011). *Opt. Express*, **19**, 175–184.

Wang, J., Chen-Wiegart, Y. & Wang, J. (2014). *Angew. Chem.* **126**, 4549–4553.

Yan, H. & Chu, Y. S. (2013). *J. Synchrotron Rad.* **20**, 89–97.

Yan, H., Conley, R., Bouet, N. & Chu, Y. S. (2014). *J. Phys. D*, **47**, 263001.

Yan, H., Kang, H., Maser, J., Macrander, A., Kewish, C., Liu, C., Conley, R. & Stephenson, G. (2007a). *Nucl. Instrum. Methods Phys. Res. A*, **582**, 126–128.

Yan, H., Maser, J., Kang, H. C., Macrander, A. & Stephenson, B. (2008). *Proc. SPIE*, **7077**, 70770Q.

Yan, H., Maser, J., Macrander, A., Shen, Q., Vogt, S., Stephenson, G. B. & Kang, H. C. (2007b). *Phys. Rev. B*, **76**, 115438.

Yan, H., Rose, V., Shu, D., Lima, E., Kang, H. C., Conley, R., Liu, C., Jahedi, N., Macrander, A. T., Stephenson, G. B., Holt, M., Chu, Y. S., Lu, M. & Maser, J. (2011). *Opt. Express*, **19**, 15069–15076.